

# Evidence for a Type 1/Type 2 dichotomy in the correlation between quasar optical polarization and host galaxy/extended emission position angles<sup>★</sup>

B. Borguet<sup>1,★★</sup>, D. Hutsemékers<sup>1,\*\*\*</sup>, G. Letawe<sup>1</sup>, Y. Letawe<sup>1</sup>, and P. Magain<sup>1</sup>

Institut d'Astrophysique et de Géophysique, University of Liège, Allée du 6 Août 17, B-4000 Liège  
e-mail: b.borguet@ulg.ac.be

Received ; accepted

## ABSTRACT

**Aims.** For Seyfert galaxies, the AGN unification model provides a simple and well established explanation of the Type 1/Type 2 dichotomy through orientation based effects. The generalization of this unification model to the higher luminosity AGNs that are the quasars remains a key question. The recent detection of Type 2 Radio-Quiet quasars seems to support such an extension. We propose to further test this scenario.

**Methods.** On the basis of a compilation of quasar host galaxy position angles consisting of previously published data and of new measurements performed using HST Archive images, we investigate the possible existence of a correlation between the linear polarization position angle and the host galaxy/extended emission position angle of quasars.

**Results.** We find that the orientation of the rest-frame UV/blue extended emission is correlated to the direction of the quasar polarization. For Type 1 quasars, the polarization is aligned with the extended UV/blue emission while these two quantities are perpendicular in Type 2 objects. This result is independent of the quasar radio-loudness. We interpret this (anti-)alignment effect in terms of scattering in a two-component polar+equatorial model which applies to both Type 1 and Type 2 objects. Moreover the orientation of the polarization –and then of the UV/blue scattered light– does not appear correlated to the major axis of the stellar component of the host galaxy measured from near-IR images.

**Conclusions.**

**Key words.** quasars: general – polarization

## 1. Introduction

The study of quasars shows that we can classify them among various categories. Radio-Loud quasars (RLQ) are distinguished from the Radio-Quiet quasars (RQQ) according to their radio power (Kellerman et al. 1989), and the Type 1/Type 2 objects from the presence or absence of broad emission lines in their spectrum (Lawrence 1987).

One can then wonder whether there exists a common link between all these objects, i.e. are the physical processes at the origin of all quasars the same? An interesting way to tackle this question consists in the use of the linear optical polarization. Polarimetry, in combination with spectroscopy, has led to major advances in the development of a unified scheme for AGN (see Antonucci 1993 for a review). The discovery of hidden broad emission lines in the polarized spectrum of the Type 2 Seyfert galaxy NGC1068 led to consider these objects as intrinsically identical to Type 1 Seyfert, the edge-on orientation of a dusty torus blocking the direct view of the central engine and the broad emission line region (Antonucci & Miller 1985).

The question we investigate in this paper relates to the possible existence of a correlation between the optical polarization position angle  $\theta_{Pola}$ <sup>1</sup> and the orientation of the host galaxy/extended emission  $PA_{host}$ <sup>2</sup> in the case of RLQs and RQQs. The relation between quasars and their host galaxies may play a fundamental role in our understanding of the AGN phenomenon and in determining the importance of the feedback of AGN on their hosts.

Such a correlation has already been studied in the case of the less powerful AGN that are the Seyfert galaxies. Thompson & Martin (1988) found a tendency for Seyfert 1 to have their polarization angle aligned with the major axis of their host galaxy, an observation that they interpreted as due to dichroic extinction by aligned dust grains in the Seyfert host galaxy. In the case of the more powerful AGN that are quasars, Berriman et al. (1990) investigated this question. They determined by hand the  $PA_{host}$  of 24 PG quasars from ground based images and computed the acute angle  $\Delta\theta$  between  $\theta_{Pola}$  and  $PA_{host}$ . They observed that while more objects seem to appear at small values ( $\Delta\theta \leq 45^\circ$ ), this effect was only marginally statistically significant.

Send offprint requests to: B. Borguet

<sup>★</sup> Table 6 is only available in electronic form at the CDS via anonymous ftp to cdsarc.u-strasbg.fr.

<sup>★★</sup> PhD. grant student of the Belgian National Fund for Scientific Research (F.N.R.S.)

<sup>\*\*\*</sup> Senior research associate F.N.R.S.

<sup>1</sup> The polarization position angle  $\theta_{Pola}$  is defined as the position angle of the maximal elongation of the electric vector in the plane of polarization, measured in degrees East of North.

<sup>2</sup> The orientation of the host galaxy  $PA_{host}$  is characterized by the position angle of its major axis projected onto the plane of the sky, measured in degrees East of North.

Investigating this problem with ground based data for Type 1 quasars is hampered by the inability of separating the faint host galaxy/extended emission<sup>3</sup> from the blinding light of the quasar nucleus. Because of its high angular resolution and stable Point Spread Function (PSF), the Hubble Space Telescope (HST) permits to properly remove the contribution of the powerful quasar nucleus thus allowing the investigation of the host galaxy parameters. A large number of quasar host observing programs were carried out with the HST leading to a statistically useful sample of quasar host galaxy parameters (e.g. Bahcall et al. 1997; Dunlop et al. 2003 and many more see Sects. 2 and 3.1). Our aim is to investigate the  $\theta_{Pola}/PA_{host}$  relation on the basis of high resolution HST quasar images. We will use either position angles given in the literature or  $PA_{host}$  we measured ourselves from HST Archive observations (hereafter called “new  $PA_{host}$  data”).

The layout of this paper is as follows. In Sect. 2 we introduce the samples of quasars used in this study which possess a  $PA_{host}$  given in the literature. In Sect. 3, we outline the samples with good imaging data but for which no  $PA_{host}$  were published, and we summarize our data analysis process and the approach followed to model the HST Archive images and to derive the host galaxy parameters. In Sect. 4 we briefly describe the polarization and radio data. Then in Sect. 5 we present the statistical analysis of the sample and the results obtained. In Sect. 6 we discuss the results and compare them to former studies. Finally, our conclusions are summarized in Sect. 7.

## 2. Description of the sample : published data

In this section we give details about the observing campaigns used in the present study excepting the new  $PA_{host}$  data which will be discussed in the next section. Note that our study is essentially based on intrinsically high luminosity Radio-Loud and Radio-Quiet AGN (i.e. quasars), but does not consider BLLac objects since these objects show highly variable luminosity and polarization (e.g. Urry & Padovani 1995). We also select the Type 2 counterpart of Radio-Loud quasars (the Narrow Line Radio Galaxies, NLRGs, Barthel 1989) from the whole RG sample on the basis of classifications given in the literature (Grandi et al. 2006; Haas et al. 2005; Cohen et al. 1999; Rudy et al. 1983; Tadhunter et al. 1998; Tadhunter et al. 2002; van Bemmelen & Bertoldi 2001; Siebenmorgen et al. 2004 and Jackson & Rawlings 1997).

In the following we present the samples which were analyzed in the literature and the methods used by authors to recover the host galaxy parameters from the quasar images. For more suitability in the following text, we take the convention to speak of the data of *Ba97* to refer to the images/data published in the paper of Bahcall et al. (1997), and so on for the other papers.

Note that in our final sample, we only consider objects from these samples if they actually possess both a reliable host position angle and an accurate enough polarization angle. So only part of the objects presented in the papers belongs to our final sample. A detailed description of the observations and  $PA_{host}$  measurements is available in Appendix A.1.

**The visible domain :** this sample is constituted of data published in the following papers, chronologically ordered : Cimatti et al. 1993, Disney et al. 1995, de Koff et al. 1996, Lehnert et al.

1999, Martel et al. 1999, Dunlop et al. 2003, Floyd et al. 2004 and McLure et al. 2004, respectively abbreviated *Ci93*, *Di95*, *Dk96*, *Le99*, *Ma99*, *Du03*, *Fl04* and *Mc04*.

The radio galaxy and quasar images studied in these papers were mostly (except the RGs from *Ci93*) imaged through an R-band filter with the HST WFPC2 camera. The sample spans a redshift range from  $z = 0.0$  to  $z = 2.0$  and is essentially made out of 3CR and PG objects. Considering these samples, we obtain a final number of 79 objects possessing a published  $PA_{host}$  in the visible domain together with a polarization position angle.

**The near-IR domain :** the near-IR compilation contains several samples coming from surveys using the NICMOS HST camera or ground based images. All the targets of the resulting sample were observed in the near-IR using K and H-band filters. The host galaxy data were retrieved from the papers of Taylor et al. 1996, Percival et al. 2001, Guyon et al. 2006 and Veilleux et al. 2006 abbreviated respectively *Ta96*, *Pe01*, *Gu06* and *Ve06*. The compiled resulting sample, considering only the objects for which we have at least a  $PA_{host}$  and a polarization position angle contains 21 objects with redshifts  $z \leq 0.4$ .

**Determination of the  $PA_{host}$  :** the  $PA_{host}$  published in the aforementioned papers were measured as follows. The first step to determine the position angle of a quasar host galaxy is the proper subtraction of the bright central source which dominates the optical emission of Type 1 objects. To this aim, a careful PSF construction is realized in order to precisely characterize the profile of a point like source imaged by a given instrument. This PSF is then scaled to the quasar intensity and subtracted from the quasar image allowing in most cases the detection of the underlying host. This first step is realized for all quasars except for Type 2 objects in which the heavy obscuration of the central source provides a non-contaminated view of the host.

Several techniques are then used to derive the host parameters ( $PA_{host}$  and  $b/a$ ) either ellipse fitting on the host image followed by the measurement of the model position angle at a chosen surface brightness, or two-dimensional galaxy profile fitting over the nucleus-subtracted image. These techniques give rather similar results since the crucial step remains the proper separation between the point-like component and the underlying host.

## 3. Measurements of new $PA_{host}$

### 3.1. The samples

The samples are constituted of available quasar/RG HST observations retrieved from the Archive, but for which the images and more particularly the host galaxy parameters were not thoroughly studied or published in the literature. Detailed observational properties of these samples are available in Appendix A.2, while major properties are summarized in Table 1.

**The visible domain :** this sample gathers quasars imaged in the V to R-band using the HST WFPC2 or ACS camera. The total sample consists of 53 objects coming from the following papers: Bahcall et al. 1997, Boyce et al. 1998, Marble et al. 2003 and Zakamska et al. 2006 hereafter abbreviated *Ba97*, *Bo98*, *Ma03* and *Za06* respectively. This sample essentially contains  $z \leq 0.5$  3CR, 2-Micron All Sky Survey (2MASS), Sloan Digital Sky Survey (SDSS) and PG quasars.

<sup>3</sup> In the following, we use indifferently the term host galaxy or extended emission to refer to all the extended emission around the central source including stars, ionized gas or scattered light.

**Table 1.** Characteristics of the surveys used to derive new host galaxy position angles.

Reference <sup>a</sup>	Prop ID <sup>b</sup>	Instrument <sup>c</sup>	Filter <sup>d</sup>
<i>Ba97</i>	5343,5099	WFPC2-WF3	F606M
<i>Bo98</i>	6303,5143	WFPC2-PC1	F702M
<i>M101</i>	7421	NICMOS-NIC2	F160M
<i>Ku01</i>	7447	NICMOS-NIC1	F110M&F165M
<i>Ma03</i>	9057	WFPC2-PC1	F814M
<i>Za06</i>	9905	ACS-WFC	F550M

<sup>a</sup> Reference to the paper where the images were published.<sup>b</sup> Corresponding HST Proposal ID.<sup>c</sup> Name of the camera.<sup>d</sup> Name of the filter used.

The near-IR domain : this sample is a compilation of 17 RQQs and RLQs from the McLeod et al. 2001 and Kukula et al. 2001 papers (hereafter abbreviated *M101* and *Ku01*). The objects, spanning a redshift range  $0.1 < z < 2.0$  were observed through the H or J-band by the NICMOS camera on board of HST.

### 3.2. The method

Here we describe the method we used to derive host galaxy position angle and axial ratio from the images. First we outline the images reduction steps and then we give an overview of the technique used to disentangle the quasar nuclear and host galaxy contributions. We then present the construction of the Point Spread Function (PSF) necessary for an accurate separation. The results of the modelling are finally given and compared to the results of other studies in the following subsection.

#### 3.2.1. Image reduction

The quasar images were retrieved from the MAST HST Archive of the Space Telescope Science Institute (STScI, <http://archive.stsci.edu/astro>). All the images are already pre-processed by standard STSDAS pipeline softwares adapted to each HST instrument. This pre-processing essentially consists in dark frame and bias subtraction along with flat-fielding, with the best reference files available. In the case of the ACS images, where the geometric distortion in the WFC camera is significant, an additional step was added to correct these distortions thanks to the *MultiDrizzle* routine (Koekemoer et al. 2002).

In addition to this pre-processing, we carried out two additional processing steps. The first consists in the removal of cosmic rays using the *crrej* task of the Image Reduction and Analysis Facility (IRAF) software which rejects high pixels from sets of exposures of the same field in an iterative way. These bad pixels are not used in the creation of the output image providing a final cosmic ray free image. In the case of the NICMOS data, this step is not essential since the MULTIACCUM mode used in the image acquisition phase already realizes this processing when acquiring the data (Schultz et al. 2005).

The second step consists in the background subtraction. As the backgrounds on the WFPC2 and ACS WFC camera are extremely flat around the targets of interest we simply estimated the mean of the background level in each image from several subset of pixels excluding obvious sources, and then subtracted this mean value to each pixel of the image. In the case of the NICMOS data, the known pedestal effect (variable quadrant bias

of the detectors) was not taken into account since the objects images were always almost centered in one of the quadrants.

#### 3.2.2. Image processing

As our primarily aim is to determine the position angle of the host galaxy surrounding nuclear dominated objects, we have to distinguish the faint fuzz of the galaxy from the quasar. The use of high resolution HST images partly solves this problem, but rises another one : the complex path of the light rays in the instrument create a complex PSF with quite extended wings that can cover, scaled to the intensity of the quasar, the underlying galaxy. The use of a deconvolution technique makes it possible to separate quite efficiently the light of the point like quasar central source (roughly a scaled PSF) from the light of the host. We used a version of the MCS algorithm (Magain et al. 1998) that is well suited to deconvolve the HST images while adjusting an analytical galaxy model.

Our image processing proceeds in essentially two steps. In the first stage, the parameters (intensity and position) of the point source are adjusted to subtract the contribution of the quasar. This contribution is estimated so that a minimal amount of PSF structure remains in the image. This step has to be realized with particular care as the inner pixels (out to a radius of 5 pixels for the extreme cases) of the quasar image may be saturated, so that the PSF subtraction process may become quite subjective.

The second stage corresponds to the fitting of an analytical galaxy profile (properly convolved with the HST PSF) to the PSF subtracted images. The analytic profile we used consists in a typical Sérsic (Sérsic 1968) profile:

$$I(x, y) = I_0 e^{-(Ax^2 + By^2 + Cxy)^\alpha} \quad (1)$$

where  $I_0$  stands for the central surface brightness, and  $\alpha$  describes its profile (the profile is called elliptical or *de Vaucouleurs* if  $\alpha = 1/8$  and spiral or disk-like if  $\alpha = 1/2$ ). A coordinate change allows us to recover the axial ratio ( $b/a$ ) and the position angle ( $PA_{host}$ ) of the model fitted to the data. Since we are essentially interested in the orientation of the major light concentration, we only use in the following a *de Vaucouleurs* profile, noting after some tests that  $PA_{host}$  does not strongly depend on  $\alpha$ .

#### 3.2.3. PSF creation

The quality of the image processing critically depends on the accuracy of the PSF used. A careful construction of the PSF is of prime importance to properly separate the contribution of the bright nucleus from that of the host galaxy. In the MCS method adapted to HST images, the construction of the PSF proceeds in two steps. The first step consists in the fitting of a sub-sampled numerical estimate of the PSF computed with the TinyTim package (Krist & Hook 2004) to an original resolution one (also estimated with TinyTim). This step provides the *Tinydec* i.e. a PSF that has a better resolution than the observed one. The second step consists in a second fit, where the *Tinydec* is fitted to an observed PSF (typically a calibration star lying in a weakly crowded field) in order to improve the agreement between the numerical estimate and the observed point source. This second fit is important since the TinyTim package is unable to give an accurate estimation of the external fainter halo ( $r > 2''$ ) as well as of the diffraction spikes (McLure et al. 2000; Pian et al. 2002).

Usually one or more stars were imaged during each of the considered campaigns with growing exposures times, allowing

the construction of a deep unsaturated PSF star. The aforementioned procedure could not be used in the case of the *Ma03* and *Za06* campaigns since no time was devoted to the observation of a specific PSF star, then forcing us to use the *Tinydec* as the PSF. However the lack of observed standard PSF star is less constraining in these two cases since the quasars imaged are generally heavily obscured objects such that the central source contribution and the intensity of the associated scattered halo are weak (or null for the Type 2 objects of *Za06*).

### 3.2.4. The error frame

In order to determine whether a given quasar model provides an accurate description of an observed image, a  $\chi^2$  minimization is used by the MCS program :

$$\chi^2 = \sum_{\text{all pixels}} \left[ \frac{\text{Image} - (\text{PointSource} + \text{Host}) \otimes \text{PSF}}{\sigma} \right]^2, \quad (2)$$

where *Image* represents the reduced quasar image, *PointSource* + *Host* the quasar model, and  $\sigma$  the standard deviation in the corresponding pixel (called the error frame). A careful construction of the error frame is mandatory for each image in order to avoid biased results.

The error term accounts for different elements : first, for a Poissonian component due to photon shot noise and dark current as well as the noise induced by the CCD readout. The second component accounts for the detector pixels that are known to work badly, these pixels being indexed in flag frames available via the STScI website. We used this frame to construct masks such that zero weight (i.e.  $1/\sigma = 0$ ) is allocated to these indexed pixels while this value is set to one everywhere else over the frame. The last component accounts for saturated regions in the observed image due to the long exposure time required for the imaging of the faint host galaxies. We accounted for this final component by assigning a null weight to the implied pixels. These masks are then multiplied by the original  $1/\sigma$  constructed in the first step.

### 3.3. The resulting $PA_{\text{host}}$

The results of our image analysis are summarized in Table 2. Columns are as follows : (1) object name, (2) redshift of the object, (3) radio-loudness of the object (RL or RQ), (4) source of the image, (5) spectral domain of the image (visible (Vis) or near-IR (NIR)), (6) type of the host galaxy (E : elliptical, S : spiral and U : undefined), (7) and (8) axial ratio and position angle of the host ( $PA_{\text{host}}$  in degrees, East of North) and (9) a quality criterion (1, 2 or 3, with 1 being the highest quality). The parameters in Col. (6) and Col. (9) are defined in the following subsections.

Fig. 1 illustrates the results for two representative objects of our *new  $PA_{\text{host}}$*  data sample. From left to right, we show for each object the final reduced HST image, a closer view on the PSF-subtracted image, the host galaxy model fitted over the PSF-subtracted image and the model-subtracted residual image (darker regions account for un-modelled details such as spiral arms, interaction features etc.).

#### 3.3.1. Morphology of the host

As we use only a *de Vaucouleurs* model to derive the host galaxy parameters, we can not provide a host morphology classification

on the basis of a better description of the host by a spheroidal or a disc-like profile. The morphological classification was thus realized by careful visual inspection of both the PSF-subtracted image and the model-subtracted residual image. We adopt a classification scheme similar to the one defined in Guyon et al. (2006) : if a bar or spiral arms are obvious in one image, the host is classified as a Spiral (disk-present) and abbreviated by S in Table 2. If no spiral structure or bar are visible in the image, we classify the host as an Elliptical galaxy (E). The remaining host galaxies (those presenting strong interaction traces/complex morphology, multiple nuclei, etc.) were assigned to the “undefined” class (abbreviated U). Finally, in some cases no host galaxy was detected even after PSF-subtraction, essentially due to the comparatively high redshift or to the insensitivity to low surface brightness features due to short exposure times.

#### 3.3.2. Reliability and error estimates

The  $b/a$  and  $PA_{\text{host}}$  reported in Table 2 are determined within uncertainties that essentially come from the degeneracy existing between the host galaxy model and the estimated nuclear contribution. These uncertainties are quite difficult to estimate, especially in our case where the objects come from samples with different observational circumstances.

A useful test to estimate the uncertainties of the derived parameters was proposed in *F104* : to ensure that the modelling routines of the host reach the global minimum within the six-dimensional model parameter space, they used six different starting point for each object close to the best-fitting parameter value. Using the same method, we checked the quality of the determination of the host parameters by starting the MCS host modelling routine with initial parameters which progressively departs from the parameter set we found during the first modelling of each object. This enabled us to also check the stability of the solution found.

This procedure allowed us to distinguish three cases that we relate to a quality criterion (Col. (9) in Table 2). The first, called 1, accounts for situations where the modelling algorithm converges towards similar solutions whatever the starting point used, then giving reliable host parameters. The second, noted 2, corresponds to the cases where the solution strongly depends upon the initial parameters (generally corresponding to the faintest/rounder hosts). The last one, noted 3, is attributed to the cases where we detect no host galaxy after the PSF-subtraction step.

Moreover, we have also considered among our sample of *new  $PA_{\text{host}}$*  data five objects which already had a  $PA_{\text{host}}$  determined in the literature. We find a good agreement<sup>4</sup> between the previously published parameters and the one we derived, assessing the capability of the method used in our study to recover host galaxy parameters. This is not a surprise since the crucial step in the  $PA_{\text{host}}$  determination essentially lies in the proper subtraction of the quasar nucleus, a step which is carefully carried out for each of the objects of our compilation (see Sect. 2). Finally we also carried out simple ellipse fitting on the nuclear-subtracted images and we observed that the derived  $PA_{\text{host}}$  agree (within  $10^\circ$ ) with those derived using the 2D profile fitting procedure described in Sect. 3.2.2. On the other hand the axial ratio  $b/a$  is more sensitive to the PSF subtraction and then not reliable enough to be used in the study. Therefore, in the following, we only use  $b/a$  to cut the sample (cf. Sect. 5).

<sup>4</sup> We find  $\Delta PA_{\text{host}}$  within  $10^\circ$  for the class 1 quality objects, see Appendix B for more details.

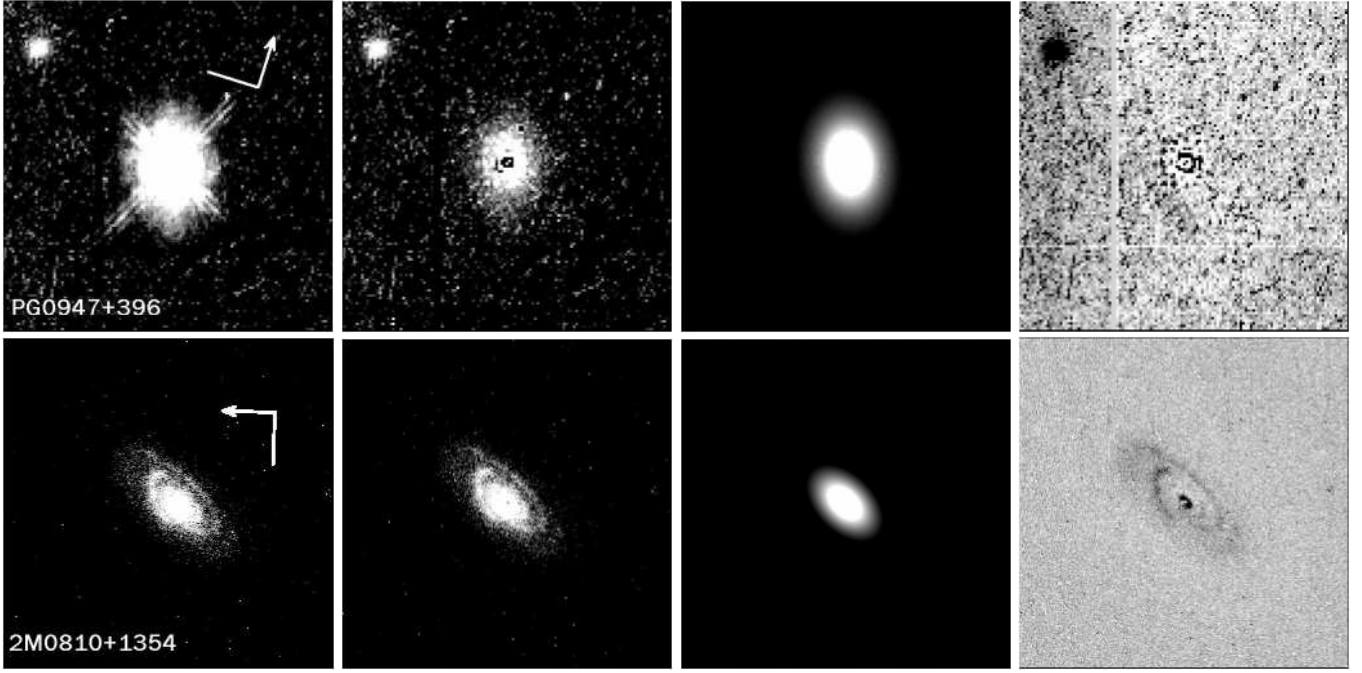


**Fig. 1.** Typical image analysis process and results for two representative objects of our sample (see text for details). North and East are marked on the left most frames (with the arrow pointing to the North). The top series of images presents one of the RQQs observed in the near-IR domain by *MI01* : PG 0947+396. It shows that the PSF subtraction step is of prime importance to characterize the faint underlying host. The bottom series present the WFC2 imaged 2M 000810+1354 RQQ by *Ma03*, hosted in a spiral galaxy.

## 4. Polarimetric and radio data

### 4.1. The polarimetric data

Most polarimetric data (the degree of polarization  $P$  and the polarization angle  $\theta_{Pola}$ ) are taken from a compilation of measurements from the literature (Hutsemékers et al. 2005). The polarimetric measurements for the objects of the sample of *Za06* were published in their paper. For the 2-MASS reddened objects of the *Ma03* sample, the polarimetric data are taken from Smith et al. (2002).

From this compilation we only considered and used data for objects where significant polarization is detected (i.e. such that  $P/\sigma_P \geq 2$ ). This also ensures that we only select data for which the polarization angle is known with an uncertainty of  $\sigma_{\theta_{Pola}} \leq 14^\circ$ .

### 4.2. The radio data

For each of the objects from our compilation which possess a  $PA_{host}$  and a  $\theta_{Pola}$ , we searched in the literature for radio data. The radio data, referring to the RLQs, consists of radio-jet position angles  $PA_{Radio}$  determined on the basis of published Very Large Array (VLA) maps from the literature. The position angle  $PA_{Radio}$  refers to the orientation defined by the axis of the prominent jet (when seen), otherwise it is the position angle of the large scale radio morphology (brightest hotspot, outer lobes) relative to the core. As for the optical and near-IR  $PA_{host}$ , the angles are computed in degrees East of North.

A large part of the Type 1 RLQ radio data comes from the measurements realized by *Le99*. Other Type 1 RLQ radio-jet data were found in the literature for several quasars (Table 3). In the case of the Type 2 RLQs, the data come from the papers of *Ci93*, *Dk96* and *Ma99* and essentially consist in compilations

of VLA/Multi Element Radio Linked Interferometer Network (MERLIN) surveys measurements from the literature.

## 5. Search for correlations

The Table 6 with all data is available on-line. For the analysis, we select the objects for which the data are relevant and accurate. Let us quickly summarize the criteria we use.

1. We do not consider Seyfert galaxies in this study. To avoid these objects, we only consider objects with  $M_V \lesssim -23$  in the Véron catalogue version 12 (Véron-Cetty & Véron 2006). Two objects (0204+292 (*Du03*,  $M_V = -22.4$ ) and 2344+184 (*Du03*,  $M_V = -22.0$ )) are then excluded from our sample. Two objects at the borderline (1635+119 (*Du03*,  $M_V = -22.8$ ) and 0906+430 (*Le99*,  $M_V = -22.9$ )) are kept. This  $M_V \lesssim -23$  criterion can not be crudely applied to the reddened objects of *Ma03* and the Type 2 Radio-Quiet objects of *Za06* since the luminosity of those objects is attenuated in the V-band. However, their high luminosity in the K-band or in the [O III] emission lines testifies their membership to the intrinsically luminous quasar sample.
2. We decided to fix an axial ratio limit  $b/a < 0.9$  in order to eliminate the roundest host galaxy morphology for which no accurate  $PA_{host}$  determination could be obtained.
3. When several data were available for a given object parameter, we always selected the value with the smallest uncertainty.
4. For consistency, we always preferred data coming from larger homogeneous samples to those selected from smaller ones.

**Table 3.** Radio data for the Type 1 RLQs of our compilation which possess known  $PA_{host}$  and  $\theta_{Pola}$ .

Name (B1950)	Catalog Name	$z$	$PA_{Radio}^a$ ( $^\circ$ )	Ref. <sup>b</sup>
0133+207	3C 47.0	0.425	35	<i>Le99</i>
0137+012	4C 01.04	0.258	30	5,6,7
0340+048	3C 393.0	0.357	40	<i>Le99</i>
0518+165	3C 138.0	0.759	70	<i>Le99</i>
0538+498	3C 147.0	0.545	60	<i>Le99</i>
0710+118	3C 175.0	0.770	60	<i>Le99</i>
0723+679	3C 179.0	0.846	90	<i>Le99</i>
0740+380	3C 186.0	1.067	140	<i>Le99</i>
0758+143	3C 190.0	1.195	30	<i>Le99</i>
0906+430	3C 216.0	0.670	40	<i>Le99</i>
1020-103	...	0.197	155	5,9
1100+772	3C 249.1	0.311	100	<i>Le99</i>
1111+408	3C 254.0	0.736	110	<i>Le99</i>
1137+660	3C 263.0	0.646	110	<i>Le99</i>
1150+497	4C 49.22	0.334	15	4,8
1226+023	3C 273.0	0.158	60	10
1250+568	3C 277.1	0.320	130	<i>Le99</i>
1302-102	...	0.286	25	10
1416+067	3C 298.0	1.436	90	<i>Le99</i>
1458+718	3C 309.1	0.905	145	<i>Le99</i>
1545+210	3C 323.1	0.266	20	3,9
1618+177	3C 334.0	0.555	140	<i>Le99</i>
1704+608	3C 351.0	0.371	40	1,2,4
1828+487	3C 380.0	0.692	135	<i>Le99</i>
2120+168	3C 432.0	1.785	135	<i>Le99</i>
2135-147	...	0.200	100	9
2247+140	4C 14.82	0.237	35	5

<sup>a</sup>  $PA_{Radio}$  measured in degrees East of North.<sup>b</sup> References. (1) Bridle et al. 1994; (2) Price et al. 1993; (3) Bogers et al. 1994; (4) Reid et al. 1995; (5) Lister et al. 1994; (6) Hintzen et al. 1983; (7) Gower & Hutchings 1984a; (8) Owen & Pushell 1984; (9) Gower & Hutchings 1984b; (10) Readhead et al. 1979.

### 5.1. The $PA_{host} - \theta_{Pola}$ correlation

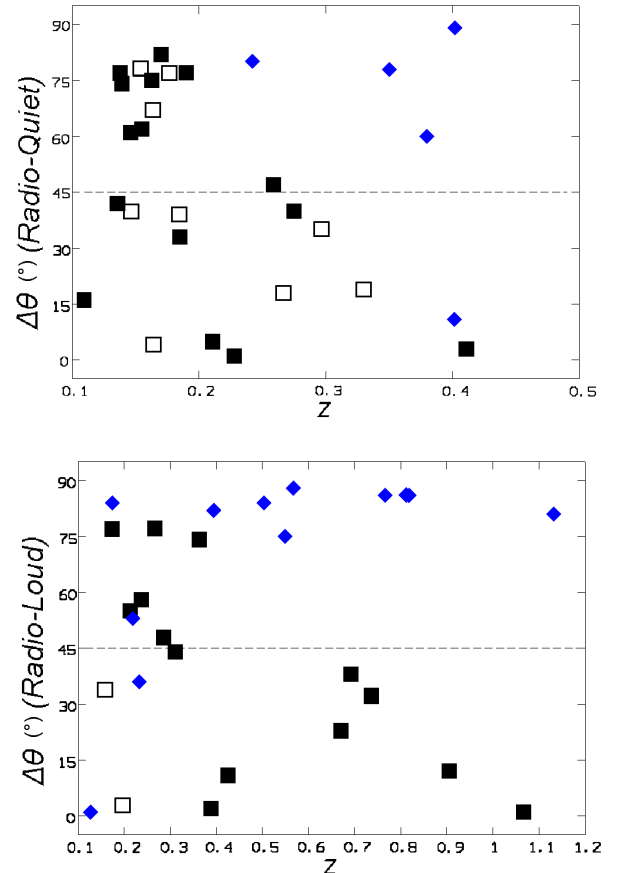
Here we consider the host galaxy data that were derived using observations taken in the visible domain ( $\lambda_{obs} \sim 6000 \text{ \AA}$ ). The data obtained in the near-IR are discussed at the end of this section. We define  $\Delta\theta$  as the acute angle between the polarization position angle  $\theta_{Pola}$  and the host galaxy orientation  $PA_{host}$  in the visible :  $\Delta\theta = 90 - |90 - |\theta_{Pola} - PA_{host}||$ . Its value is defined between 0 and 90 degrees.

#### 5.1.1. The Radio-quiet objects

The upper panel of Fig. 2 summarizes the  $\Delta\theta$  behavior as a function of the redshift for both Type 1 and Type 2 RQQ objects in our sample. While at small redshifts there seems to be no clear correlation between  $\theta_{Pola}$  and  $PA_{host}$  for Type 1 objects (the redshift extent of the Type 2 RQQ sample is too limited to conclude), a distinct separation between the Type 1 and Type 2 behavior is noted for objects lying at larger redshifts ( $z \gtrsim 0.2 - 0.3$ ) where the polarization position angle of Type 1 objects is preferentially parallel to the host major axis (“alignment” :  $\Delta\theta \leq 45^\circ$ ) while the polarization is mostly perpendicular to the host major axis in Type 2 quasars (“anti-alignment” :  $\Delta\theta \geq 45^\circ$ ). We also observe this type of behavior if we only consider the more polarized objects ( $P \geq 0.6\%$  pictured by filled symbols). It is worth noting that the 2MASS reddened quasars from the *Ma03* study appear preferentially at small  $\Delta\theta$  values ( $\Delta\theta \leq 45^\circ$ ) as other un-

**Table 4.** Results of the two sample Kolmogorov-Smirnov test applied to the  $\Delta\theta$  distribution of Type 1 and Type 2 quasars.

Selected Sample <sup>a</sup>	$N_1^b$	$N_2^c$	$P_{K-S}^d$ (%)
RQ	24	5	7.24
RQ ( $P \geq 0.6\%$ )	15	5	15.75
RQ ( $z \geq 0.2$ )	8	5	0.11
RQ ( $P \geq 0.6\% \& z \geq 0.2$ )	5	5	0.37
RL	16	16	2.30
RL ( $P \geq 0.6\%$ )	14	15	1.95
RL ( $z \geq 0.2$ )	13	10	0.23
RL ( $P \geq 0.6\% \& z \geq 0.2$ )	13	10	0.23
RQ+RL	40	21	0.24
RQ+RL ( $P \geq 0.6\%$ )	29	20	0.21
RQ+RL ( $z \geq 0.2$ )	21	15	0.01
RQ+RL ( $P \geq 0.6\% \& z \geq 0.2$ )	18	15	0.03

<sup>a</sup> Criteria used to define sub-samples.<sup>b</sup> Size of the selected Type 1 subsample.<sup>c</sup> Size of the selected Type 2 subsample.<sup>d</sup> Probability  $P_{K-S}$  (in percent) that the  $\Delta\theta$  of Type 1 and Type 2 objects are selected from the same parent sample.**Fig. 2.** Distribution of the acute angle  $\Delta\theta$  between the polarization position angle  $\theta_{Pola}$  and the orientation of the host galaxy morphology  $PA_{host}$ , as a function of the redshift  $z$ . The upper panel refers to Radio-Quiet objects while the lower panel refers to Radio-Loud objects. Type 1 objects are represented in both panel by squares and Type 2 objects by diamonds. The filled symbols refer to objects with a polarization degree  $P \geq 0.6\%$ .

reddened Type 1 objects from the sample. We finally note that one Type 2 RQQ quasar at  $z = 0.402$  appears at small  $\Delta\theta$ . The behavior of this object, SDSS J0920+4531, already discussed in *Za06*, seems to be due to an unfortunate apparent superposition of a close companion galaxy leading to a biased  $PA_{\text{host}}$  determination.

In order to assess the significance of the alignment observed in the upper panel of Fig. 2 we carried out statistical tests on the Type 1 and Type 2 RQQ samples. We used the two sample non-parametric Kolmogorov-Smirnov ( $K-S$ ) test to determine if the Type 1 and Type 2  $\Delta\theta$  distributions are drawn from the same parent population. The results of the  $K-S$  tests applied to the two aforementioned samples using several selection criteria are summarized in Table 4. From these results, we can note that, while accounting for the whole RQQ sample does not allow an effective distinction between the Type 1 and Type 2 parent sample, the selection of the higher redshift objects ( $z \geq 0.2$ ) shows that the probability that the difference in the  $\Delta\theta$  behavior seen among the two samples is fortuitous is of only 0.11 %. The same conclusions can be reached if we only consider the more polarized objects ( $P \geq 0.6\%$ ) but with a weaker statistical significance as the selected sample becomes smaller.

We also investigated the variation of  $\Delta\theta$  as a function of the redshift considering Type 1 and Type 2 objects separately. To this aim, we performed a non parametric *Kendall- $\tau$*  rank test on the Type 1 RQQ sample in order to check the strength of the correlation between the alignment ( $\Delta\theta$ ) and the redshift. This statistical test uses the relative order of ranks in a data set to determine the likelihood of a correlation. We found a 4% probability that the anti-correlation between the  $\Delta\theta$  and the redshift is purely fortuitous in the case of the Type 1 RQQ sample. We do not carry this test on our Type 2 RQQ sample given its limited redshift range.

### 5.1.2. The Radio-loud objects

The  $\Delta\theta$  relation is also studied in the case of the Radio-Loud sample. The lower panel of Fig. 2 illustrates the observed  $\Delta\theta$  behavior in this case. Once again, the  $\Delta\theta$  distribution is clearly non-random. A first look allows to see that the Type 1 RLQs are preferentially found at small  $\Delta\theta$  (i.e. alignment between the polarization angle and the major axis of the host). Type 2 objects often exhibit large offset angles,  $\Delta\theta \geq 45^\circ$ , indicating an anti-alignment between the polarization angle and the host galaxy position angle (Cimatti et al. 1993).

The lower panel of Fig. 2 suggests a dependence of  $\Delta\theta$  as a function of the redshift as already noted for the Type 2 RLQs (Cimatti et al. 1993). Indeed, at small redshift ( $z \leq 0.2$ ), as in the Radio-Quiet case (upper panel of Fig. 2), we do not find any particular  $\Delta\theta$  difference for either Type 1 or Type 2 objects while at higher redshift ( $z \geq 0.3 - 0.4$ ) we observe a clear separation of the  $\Delta\theta$ .

Statistical tests were carried out on the data in order to assess the strength of the (anti-)alignment. The results of a two sample  $K-S$  test using several selection criteria applied to Radio-Loud objects are summarized in Table 4. The two sample  $K-S$  test comparing the distribution of Type 1 and Type 2  $\Delta\theta$  on the whole RLQ sample shows that there is only a 2.3% probability that the  $\Delta\theta$  of the two samples are selected from the same parent distribution. More selective criteria<sup>5</sup> ( $z \geq 0.2$ ,  $P \geq 0.6\%$  or both)

<sup>5</sup> Although the alignment/anti-alignment seems to appear at higher redshift for RLQs, we keep the cutoff in the test at  $z \geq 0.2$  for consistency with RQQs. However, using a higher redshift cutoff results in even more significant correlations.

on the RLQ sample reinforce the conclusion of the statistical test.

A *Kendall- $\tau$*  correlation test considering Type 1 and Type 2 objects separately was applied to the sample in order to investigate the redshift dependency of the  $\Delta\theta$  distribution. For the Type 1 RLQs, the result of the test shows that there is a 4% probability that the anti-correlation of the  $\Delta\theta$  with the redshift is purely fortuitous while for Type 2 objects the probability that the correlation is fortuitous is only of 0.2%.

### 5.1.3. A global view

A global look at both panels of Fig. 2 suggests a similar behavior of the Type 1/Type 2 quasars whatever their radio-loudness: at  $z \geq 0.2 - 0.3$  the Type 1 objects systematically lie at small  $\Delta\theta$  having their polarization mainly parallel ( $\Delta\theta \leq 45^\circ$ ) to their morphological major axis while the Type 2 objects are found at higher offset angle ( $\Delta\theta \geq 45^\circ$ ). These observations are supported by statistical tests carried out on the mixed RQQ and RLQ sample (Table 4). The *Kendall- $\tau$*  correlation test lead to the conclusion that there is a 0.2 % probability that the correlation between  $\Delta\theta$  and  $z$  is purely fortuitous for the Type 2 quasars and of 0.4 % that the anti-correlation is fortuitous for Type 1 objects.

In order to verify that the difference in the behavior of  $\Delta\theta$  between Type 1 and Type 2 quasars actually corresponds to alignment and anti-alignment respectively, we computed the mean value  $\overline{\Delta\theta}$  of the  $\Delta\theta$  for both samples at  $z \geq 0.2$  separately and compared this value to the distribution of mean offset angles computed from simulated samples obtained by shuffling the  $PA_{\text{host}}$  among the objects. We found that the  $\overline{\Delta\theta} = 31^\circ$  (resp.  $\overline{\Delta\theta} = 72^\circ$ ) value measured for the Type 1 (resp. Type 2) quasars has a probability of 0.3 % (resp. 0.02 %) to occur in a random distribution of polarization and host position angles. This test was not applied to RQQ and RLQ samples separately given the small number of objects.

We also investigated the  $PA_{\text{host}} - \theta_{\text{pola}}$  correlation for the RQQ and RLQ samples using the compilation of near-IR  $PA_{\text{host}}$  data. However for those data, we do not see any clear correlations between the polarization angle and the host galaxy position angle even at higher redshifts ( $z \geq 0.2 - 0.3$ ). This lack of correlation was confirmed by the  $K-S$  and *Kendall- $\tau$*  tests.

## 5.2. Other interesting correlations

### 5.2.1. The $PA_{\text{Radio}} - \theta_{\text{pola}}$ correlation

Using the available VLA radio-jet orientation for the Radio-Loud objects of our sample possessing optical polarization measurements (Table 3 and *Ci93*), we also investigate the  $PA_{\text{Radio}} - \theta_{\text{pola}}$  correlation. We define the radio-jet/polarization offset angle in the same way as the offset defined in Sect. 5.1:  $\Delta\theta_{r-p} = 90 - |90 - |\theta_{\text{pola}} - PA_{\text{Radio}}||$  whose value is comprised between 0 and 90 degrees.

Fig. 3 synthesizes the  $\Delta\theta_{r-p}$  distribution for the Radio-Loud objects as a function of the redshift. One can note that the radio-jet of Type 1 Radio-Loud quasars are mostly aligned with the polarization ( $\Delta\theta_{r-p} \leq 45^\circ$ ) while these two directions are mostly anti-aligned in Type 2 objects ( $\Delta\theta_{r-p} \geq 45^\circ$ ). Moreover, we do not see any redshift dependence of the correlation. We carry out  $K-S$  test over the  $\Delta\theta_{r-p}$  distribution of Type 1 and Type 2 objects. The two sample  $K-S$  test shows that there is less than a 0.001 % probability that both samples are selected from the same parent distribution. This result is even more significant if we only con-



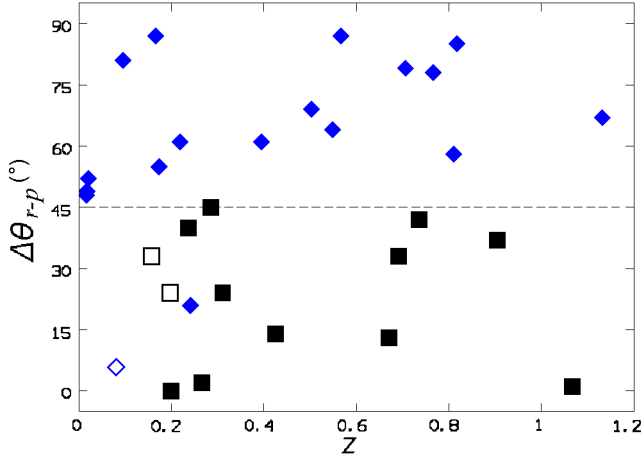


**Fig. 3.** Distribution of the acute angle  $\Delta\theta_{r-p}$  between the polarization position angle  $\theta_{Pola}$  and the orientation of the radio jet  $PA_{Radio}$  defined in Sect. 4.2. As in the other figures, Type 1 objects are represented by squares and Type 2 objects are represented by diamonds. The symbols are filled when  $P \geq 0.6\%$ .

sider the  $P \geq 0.6\%$  quasars. We also find a 0.17 % (resp. 0.06 %) probability that the  $\Delta\theta_{r-p} = 24^\circ$  measured for Type 1 RLQs (resp.  $\Delta\theta_{r-p} = 65^\circ$  for Type 2) comes from a random  $\Delta\theta_{r-p}$  distribution.

These (anti-)alignment effects were already reported previously in the literature. For the Type 1 objects, a clearly non-random distribution of  $\Delta\theta_{r-p}$  has been reported by many authors (e.g. Stockman et al. 1979; Rusk & Seaquist 1985; Berriman et al. 1990; Lister & Smith 2000), showing that the optical polarization angle of Type 1 RLQs mostly aligns with their radio-morphology. For the Type 2 Radio-Loud quasars the anti-alignment between the radio-jets and the optical polarization is known as part of the so called “*RG alignment effect*” observed in high- $z$  radio galaxies (e.g. McCarthy et al. (1987); Chambers et al. (1987); Cimatti et al. (1993)). Indeed, using polarization measurements and VLA radio observations of RGs, they found a strong anti-alignment between the linear polarization orientation and the radio structure.

### 5.2.2. The $PA_{Radio} - PA_{host}$ correlation

Using the radio-jet orientations given in Table 3 and Ci93 for the Radio-Loud objects of our sample with a reliable host galaxy position angle, we finally look at the correlation of the radio-jet with the morphology of the host. We define the offset angle  $\Delta\theta_{r-o}$  between the radio-jet and host major axis position angle using the same definition as in the preceding sections. Fig. 4 summarizes the behavior of  $\Delta\theta_{r-o}$  as a function of the redshift.

For the Type 1 RLQs, we note a significant alignment ( $P \leq 0.001\%$  that the measured  $\Delta\theta_{r-o} = 24^\circ$  is due to chance) between the host galaxy’s main orientation and the radio-jet orientation, as first reported within a larger sample in Le99. This is not a surprise since 2/3 of the Type 1 RLQ sample used to check this correlation is made of the measurements given in Le99.

For the Type 2 RLQs (the NLRGs) we also note an alignment ( $\Delta\theta_{r-o} \leq 45^\circ$ ) between the radio-jet and the host position angle. The permutation test gives a  $P \leq 8\%$  that the measured  $\Delta\theta_{r-o} = 30^\circ$  is due to chance. Although one might suspect a redshift dependence on Fig. 4, it is not significant in our sample (as

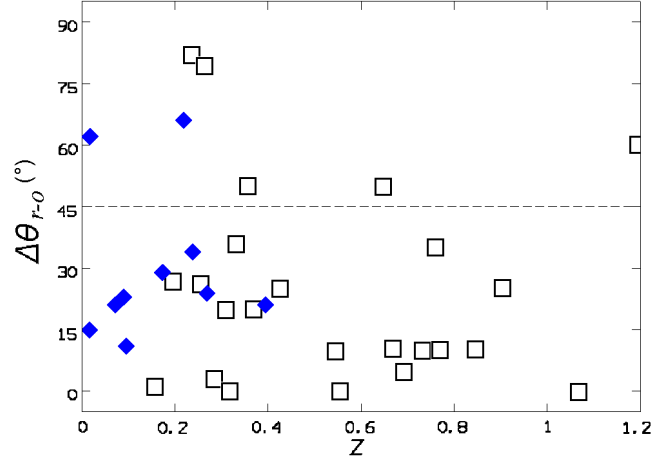


**Fig. 4.** Distribution of the acute angle  $\Delta\theta_{r-o}$  between the orientation of the radio jet  $PA_{Radio}$  and the host galaxy position angle  $PA_{host}$  in the visible domain. Type 1 objects are represented by empty squares and Type 2 objects are represented by filled diamonds.

**Table 5.** Summary of the correlations studied.

Radio Type	Correlation	Type 1 <sup>a</sup>	Type 2 <sup>a</sup>
Radio-Quiet	$PA_{host} - \theta_{Pola}$	$\parallel^{(6)}$	$\perp^{(5)}$
Radio-Loud	$PA_{host} - \theta_{Pola}$	$\parallel^{(6)}$	$\perp^{(1)}$
Radio-Loud	$\theta_{Pola} - PA_{Radio}$	$\parallel^{(3)}$	$\perp^{(1)}$
Radio-Loud	$PA_{host} - PA_{Radio}$	$\parallel^{(2,6)}$	$\parallel^{(1,4)}$

<sup>a</sup> Numbers in parentheses give the reference to the first detection of a given correlation for Type 1 and Type 2 quasars : (1) Chambers et al. 1987; McCarthy et al. 1987; Cimatti et al. 1993; (2) Le99; (3) Stockman et al. 1979; (4) Biretta et al. 2002; (5) Zakamska et al. 2006 and (6) this work.

the result of the *Kendall- $\tau$*  test). Let us notice that this alignment is known as part of the “*RG alignment effect*” (e.g. McCarthy et al. (1987); Chambers et al. (1987)) where the optical morphology of higher redshift ( $z \geq 0.5$ ) RGs aligns with the radio-jet.

### 5.3. Summary of the results

The known correlations between quasar orientation parameters are summarized in Table 5. The main result of our study is the discovery of a correlation between  $PA_{host}$  and  $\theta_{Pola}$  in quasars observed whatever their radio-loudness but depending on the spectroscopic type of the source. We find that while high redshift Type 2 quasars exhibit an anti-alignment of their optical polarization angle with their optical, rest frame UV/blue, morphology, the optical host galaxy position angle is preferentially aligned with the polarization angle in Type 1 quasars.

Another interesting result is the redshift dependence of the alignment. Indeed, as suggested by both upper and lower panels of Fig. 2 and the results of the statistical tests, the alignment becomes significant if we consider redshifts higher than  $z \sim 0.2 - 0.3$  for either Radio-Loud or Radio-Quiet objects. This observation may explain the lack of correlation observed by Berriman et al. (1990) between  $\theta_{Pola}$  and  $PA_{host}$  since the redshift extent of their sample was rather small (among their 24 objects with  $z \leq 0.4$ , only 5 of them have  $z \geq 0.3$ ). Note that the precise cutoff is not clearly determined and might be slightly higher as



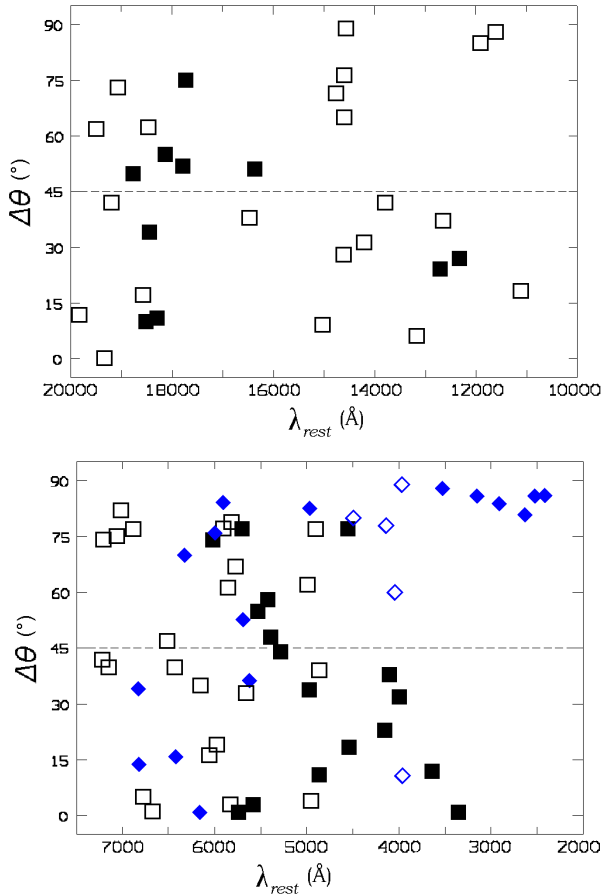


**Fig. 5.** Distribution for RQQs and RLQs of the acute angle  $\Delta\theta$  between  $PA_{host}$  and  $\theta_{Pola}$  as a function of the observation wavelength  $\lambda_{rest}$  as measured in the quasar rest-frame. The upper panel presents the  $\Delta\theta$  distribution at near-IR wavelengths while the lower panel presents the same distribution at UV/visible wavelengths. RQQs are represented by empty symbols and RLQs by filled symbols. Type 1 objects are pictured by squares while Type 2 objects are pictured by diamonds. No observations of Type 2 quasars are available in the near-IR. Our sample does not contain quasars imaged at  $7500 \text{ \AA} \leq \lambda_{rest} \leq 11000 \text{ \AA}$ .

suggested by RLQs (Fig. 2). Observations of RQQs at higher  $z$  would be needed to clarify this point.

Finally, we note that, while the alignment between the host galaxy position angle and the polarization angle is clearly observed and statistically significant in the case of the optical  $PA_{host}$  data, we do not find a similar behavior with the near-IR  $PA_{host}$  data. Optical and K-band studies of high  $z$  RGs already showed that while an alignment effect is observed between their optical emission and their radio axis, a significantly weaker alignment is observed between the K-band emission and the radio axis (Rigler et al. 1992; Dunlop & Peacock 1993; Best et al. 1998). This argues in favor of a scheme where the K-band emission is not necessarily related to the visible (rest-frame blue) light.

## 6. Discussion

### 6.1. The observed correlation

In Sect. 5 we reported on the existence of an (anti-)alignment between the linear polarization and the host galaxy position angle

of (Type 2) Type 1 quasars. We noticed that this behavior seems to be independent of the radio-loudness. It is also interesting to remind the lack of correlation in the near-IR domain and the redshift dependence of the  $PA_{host} - \theta_{Pola}$  (anti-)alignment. These last two facts lead us to think that the observed correlations might be linked to the rest-frame UV/blue part of the quasar light which is redshifted to optical wavelengths for the higher  $z$  objects. This hypothesis is supported by Fig. 5, where we plot  $\Delta\theta$  as a function of  $\lambda_{rest}$ , the rest-frame wavelength at which  $PA_{host}$  is measured (i.e. the central wavelength of the imaging filter divided by  $1+z$ ).

We note that while at longer wavelengths there is no particular behavior in the  $\Delta\theta$  distribution for either Type 1 or Type 2 objects, the (anti-)alignment effect clearly appears at shorter wavelengths ( $\lambda_{rest} \lesssim 5000 \text{ \AA}$ ). At  $\lambda_{rest} \leq 5000 \text{ \AA}$ , a two sample  $K-S$  test shows that there is a 0.01 % probability that the  $\Delta\theta$  distribution of Type 1 and Type 2 quasars is drawn from the same parent sample.

### 6.2. The UV/blue continuum and the origin of the correlation

The morphology of Type 2 Radio-Loud objects (NLRGs) has been extensively studied in the literature since those objects do not possess a bright central nucleus masking the underlying host and can be observed at high redshifts. Imaged at optical wavelengths, higher redshift RGs ( $z \geq 0.5$ ) are known to show the aforementioned “*RG alignment effect*” where the extended rest frame UV/blue continuum emission aligns with the radio-jet. This alignment, not seen in the near-IR images of the same objects (Rigler et al. 1992) leads to a two component RG model: at shorter wavelengths, the continuum is dominated by an extended UV/blue component aligned with the radio axis while at longer wavelengths, the quasar light is dominated by a stellar component which possesses the morphology and physical dimensions of elliptical galaxies.

This extended UV/blue continuum which can show a quite complex morphology (McCarthy et al. 1997) was primarily interpreted, given its alignment with the radio-jet, as massive star formation regions triggered by the shocks associated to the passage of the radio-jet through the host galaxy (McCarthy et al. 1987). However, as we briefly recalled in Sect. 5.1.2, high redshift NLRGs are also known to show an anti-alignment between their optical linear polarization and their rest frame UV/blue morphological structure (e.g. Cimatti et al. 1993; Hurt et al. 1999), supporting the possibility that at least part of this extended UV/blue light is due to the polar scattering of the light from the quasar nucleus by electrons and/or dust (di Serego Alighieri et al. 1989; Cimatti et al. 1993; di Serego Alighieri et al. 1993; Dey et al. 1996; Tadhunter et al. 2002). Indeed, this assumption provides a simple explanation to the fact that the polarization angle is perpendicular to the optical, extended rest frame UV/blue light in the host galaxy.

Due to their apparent faintness and the absence of strong radio counterpart, Type 2 Radio-Quiet quasars have long been searched for. The hard X-ray and SDSS surveys recently unveiled large samples of Type 2 RQQ candidates, showing that these objects are not extraordinarily rare (e.g. Zakamska et al. 2003 and references therein). The HST spectropolarimetric study of a sample of 12 Type 2 RQQs revealed that a large part of them (9 out of 12) possess high optical polarization and that for 5 objects their polarized spectra contain broad emission lines betraying the presence of a Type 1 nucleus (Zakamska et al. 2005). Three band HST imaging of 9 Type 2 RQQs also reveals some morphologically complex emission which appears in the bluer

images (Za06). These structures were interpreted as scattering cones since their position angle lies almost perpendicularly to the *E-vector* polarization plane. As in NLRGs, scattering in the extended UV/blue component seems to represent a viable interpretation of the origin of the detected polarization.

The detection of a hypothetical extended blue component in either Radio-Loud or Radio-Quiet Type 1 quasars is hindered by the central source whose strong contribution at smaller wavelengths remains difficult to estimate and properly subtract. However, if Type 1 and Type 2 objects are, according to the unification model, intrinsically identical, the extended scattering region resolved in Type 2 quasars should also be present, but masked by the higher apparent brightness of the unobscured central source. Since the viewing angle of Type 1 and Type 2 objects is thought to be an essential parameter controlling the observed properties of those objects, the polarization geometry may also be affected by the viewing angle. While in this framework Type 2 objects are almost seen edge-on such that the extended polar scattering regions produce a polarization angle perpendicular to the symmetry axis of the AGN (pictured by the radio-jet axis in the RLQ objects), the situation may be different in the nearly face-on Type 1 quasars.

An enticing interpretation of the polarization properties was recently proposed for the Seyfert galaxies. Indeed, Seyfert galaxies exhibit some kind of *alignment effect* between their optical linear polarization and their radio axis. While the Type 2 objects polarization is known to be anti-aligned with the radio axis (Antonucci 1983), the polarization originating from scattering cones perpendicular to the obscuring torus (Antonucci & Miller 1985), Type 1 Seyferts are found to be of both kinds (aligned and anti-aligned, Smith et al. 2002). The scenario proposed to account for these observations consists of a two component polar+equatorial scattering model (Smith et al. 2004, 2005; Goosmann et al. 2007). While the extended polar scattering region accounts for the perpendicular polarization, the much smaller equatorial disk-like component inside the obscuring torus produces a polarization which, projected onto the plane of the sky, is parallel to the symmetry axis of the system (see Fig. 6). In this framework, Type 2 polarization properties are dominated by polar scattering, the equatorial component being hidden by the dusty torus. In Type 1 objects, the smaller but significantly non-zero inclination angle of the system is such that both scattering regions contribute to the polarized flux, the resulting polarization being dominated by the equatorial scattering component (Smith et al. 2002).

This two component scattering scheme seems to nicely fit our observations as it provides an explanation to the correlations found in Sect. 5.1 assuming that the observed polarization is due to scattering (in both RQ and RL objects) and that the morphology of the host galaxy/extended emission observed in higher redshift quasars is, at least in part, related to scattered UV/blue light<sup>6</sup>. The model also provides a simple explanation of the alignment seen in Type 1 and Type 2 Radio-Loud quasars between their polarization position angle and their radio jets since the radio-jets are thought to be emitted along the symmetry axis of the accretion disk which also defines the direction of the ex-

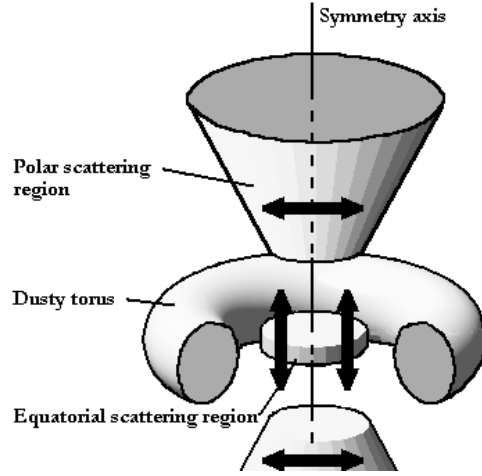


**Fig. 6.** Cartoon illustrating the adopted quasar model and more particularly the two scattering regions used to interpret our results (adapted from Smith et al. 2004). The system is shown inclined with respect to the line of sight to the observer such that a Type 1 object is seen (in Type 2 objects the dusty torus is seen edge-on and the central part is hidden). The arrows indicate the direction of the resulting polarization projected onto the plane of the sky for each scattering region (see text for more details). In RLQs, the radio jet (not illustrated) extends along the symmetry axis.

tension of the polar scattering regions. Moreover, assuming the proposed model applies and reminding the lack of correlation in the near-IR (which samples the stellar component), our observations suggest that the central engine symmetry axis and the orientation of the stellar component are not correlated. This lack of correlation has already been reported in the case of Seyfert and radio galaxies (e.g. Kinney et al. 2000 and references therein; Schmitt et al. 2001) suggesting alternative models to the fuelling of the AGN supermassive black hole (e.g. King & Pringle 2007). Our results suggest that such scenarios might also apply to the higher luminosity quasars.

Recent HST two band imaging of Type 1 RQQs (e.g. Sanchez et al. 2004; Jahnke et al. 2004) shows an enhancement of the rest frame blue light of the host galaxy with respect to normal galaxies of similar redshift and luminosity. This blue excess is actually explained as due to merger induced activity. However, those objects do not show more evidence for interaction than inactive galaxies at similar redshift and luminosity (Sanchez et al. 2004). Polarimetric study of these objects might provide an explanation of this excess blue light in terms of scattering, although an accurate estimate of the fraction of scattered light in Type 1 quasars might be difficult given the fact that the observed polarization is the combination of both polar and equatorial polarization acting in opposite ways.

Let us finally note that we also searched –without success– for a possible correlation between  $\Delta\theta$  and the quasar absolute magnitude, since the fraction of scattered over stellar light may be more important in the hosts of intrinsically more luminous quasars.

## 7. Conclusions

Using host galaxy position angles ( $PA_{\text{host}}$ ) determined from high resolution optical/near-IR images of quasars and data from the literature, we investigate the possible existence of a correlation

<sup>6</sup> Let us emphasize that only the polar scattering region –assumed to be parallel to the symmetry axis of the system– can be angularly resolved (in principle in both Type 1 and Type 2 objects). The equatorial scattering region –perpendicular to the symmetry axis– is too small to be resolved. Note that in this framework, given the projections effects and the presence of two competing scattering regions, we expect the dispersion of the  $\Delta\theta$  to be higher for Type 1 quasars than for Type 2 ones as it might be suspected in Fig. 2.

between the host morphology and the polarization direction in the case of Radio-Quiet and Radio-Loud quasars. We can summarize our results as follows :

1. We find an alignment between the direction of the linear polarization and the rest-frame UV/blue major axis of the host galaxy of Type 1 quasars. In the case of Type 2 objects, it is well established that the extended UV/blue light is correlated to the observed polarization, as these blue regions are thought to be dominated by scattering. Our results suggest that such an extended UV/blue scattering region is also present in Type 1 quasars.
2. We do not find such an alignment effect with the near-IR host morphology. This suggests that the morphology of the extended UV/blue emission is not related to the morphology of the stellar component of the host galaxy which dominates in the near-IR.
3. We observe the same  $PA_{host} - \theta_{pola}$  behavior for either Radio-Loud or Radio-Quiet objects. This observation supports the idea that the UV/blue continuum is not entirely due to star formation processes triggered by the radio-jet.
4. The observed correlation fits a unification model where the Type 1/Type 2 dichotomy is essentially determined by orientation effects assuming the two component scattering model of Smith et al. (2004, 2005). Indeed, depending on the viewing angle to the quasar, the polarization would predominantly arise from either the equatorial or the polar scattering region giving rise to the observed behavior.

In order to strengthen the conclusions and to further investigate the correlations presented in this paper, new observations of quasars in the rest-frame UV/blue domain are needed, especially of Radio-Quiet objects for which few observations at  $\lambda_{rest} \leq 5000 \text{ \AA}$  are available. The detection of the extended blue/UV continuum region and the measurement of its polarization would help to test our interpretation.

**Acknowledgements.** Part of this work was financially supported by a PAI (Pôle d'Attraction Inter-universitaire) grant (PAI 5/36) and a PhD student grant of the Belgian Fund for Scientific Research (F.N.R.S.). This work was also supported in part by PRODEX Experiment Agreement 90195 (ESA and PPS Science Policy, Belgium). Use of ADS and MAST/ESO HST archive. This research has made use of the Vizier catalogue access tool and the SIMBAD database, operated at CDS, Strasbourg, France. B.B. would like to thank V. Chantry for the help provided about reduction pipeline for HST NICMOS and ACS images, and P. Greenfield and the STScI Help Desk Staff for the councils provided for the WFPC2 image reduction. We thank the anonymous referee for useful comments and suggestions that improved the paper.

## References

- Antonucci, R. 1983, *Nature*, 303, 158  
 Antonucci, R. & Miller, J. 1985, *ApJ*, 93, 785  
 Antonucci, R. 1993, *ARA&A*, 1993.31, 473  
 Baggett, S. et al. 2002, *WFPC2 Data Handbook*, version 4.0 (Baltimore : STScI)  
 Bahcall, J.N., Kirhakos, S. & Schneider, D.P. 1996, *ApJ*, 457, 557  
 Bahcall, J.N., Kirhakos, S. & Saxe, D.H. 1997, *ApJ*, 479, 642  
 Barthel, P.D. 1989, *AJ*, 336, 606  
 Berriman, G., Schmidt, G.D., West, S.C. & Stockman, H.S. 1990, *ApJS*, 74, 869  
 Best, P.N., Longair, M.S. & Röttgering, J.A. 1998, *MNRAS*, 295, 549  
 Biretta, J.A., Martel, A.R., McMaster, M., et al. 2002, *New A Rev.*, 46, 181  
 Boges, W.J., Hes, R., Barthel, P.D. & Zensus, J.A. 1994, *A&A*, 105, 91  
 Boyce, P.J., Disney, M.J., Blades, J.C., et al. 1998, *MNRAS*, 298, 121  
 Bridle, A.H., Hough, D.H., Lonsdale, C.J., Burns, J.O. & Laing, R.A. 1994, *AJ*, 108, 766  
 Chambers, K.C., Miley, G.K. & van Breugel, W. 1987, *Nature*, 329, 604  
 Cimatti, A., di Serego-Alighieri, S., Fosbury, R.A.E., Salvati, M. & Taylor, D. 1993, *MNRAS*, 264, 421  
 Cohen, M.H., Ogle, P.M., Tran, H.D., Goodrich, R.W. & Miller, J.S. 1999, *AJ*, 118, 1963  
 de Koff, S., Baum, S.A., Sparks, W.B., et al. 1996, *ApJS*, 107, 621  
 Dey, A., Cimatti, A., van Breugel, W., Antonucci, R. & Spinrad, H. 1996, *ApJ*, 465, 157  
 di Serego Alighieri, S., Fosbury, R.A.E. 1993, Quinn P.J. & Tadhunter, C.N. 1989, *Nature*, 341, 307  
 di Serego Alighieri, S., Cimatti, A. & Fosbury, R.A.E. 1993, *ApJ*, 404, 584  
 Disney, M.J., Boyce, P.J., Blades, J.C., et al. 1995, *Nature*, 376, 150  
 Dunlop, J.S. & Peacock, J.A. 1993, *MNRAS*, 263, 936  
 Dunlop, J.S., McLure, R.J., Kukula, M.J., et al. 2003, *MNRAS*, 340, 1095  
 Floyd, D.J.E., Kukula, M.J., Dunlop, J.S., et al. 2004, *MNRAS*, 355, 196  
 Goosmann, R.W. & Gaskell, C.M. 2007, *A&A*, 465, 129  
 Gower, A.C. & Hutchings, J.B. 1984a, *PASP*, 96, 19  
 Gower, A.C. & Hutchings, J.B. 1984b, *AJ*, 89, 1658  
 Grandi, P., Malaguti, G. & Flocchi, M. 2006, *ApJ*, 642, 113  
 Guyon, O., Sanders, B.D., Stockton, A. 2006, *astro-ph/0605079v1*  
 Haas, M., Siebenmorgen, R., Shultz, B., Krügel, E. & Chini, R. 2005, *A&A*, 442, L39  
 Hao, L., Strauss, M.A., Tremonti, C.A., et al. 2005, *AJ*, 129, 1783  
 Hintzen, P., Ulvestad, J. & Owen, F. 1983, *AJ*, 88, 709  
 Hurt, T., Antonucci, R., Cohen, R., Kinney, A. & Krolik, J. 1999, *ApJ*, 514, 579  
 Hutsemekers, D., Cabanac, R., Lamy, H. & Sluse, D. 2005, *A&A*, 441, 915  
 Jackson, N. & Rawlings, S. 1997, *MNRAS*, 286, 241  
 Janhke, K., Sanchez, S.F., Wisotzki, L., et al. 2004, *AJ*, 614, 568  
 Kellerman, K.I., Sramek, R., Schmidt, M., Shaffer, D.B. & Green, R. 1989, *AJ*, 98, 1195  
 King, A.R. & Pringle, J.E. 2007, *MNRAS*, 377, L25  
 Kinney, A.L., Schmitt, H.R., Clarke, C.J., et al. 2000, *ApJ*, 537, 152  
 Koekemoer, A.M., Fruchter, A.S., Hook, R.N. & Hack, W. 2002, *HST Calibration Workshop*, eds. S. Arribas, A.M. Koekemoer & B. Whitmore (Baltimore : STScI)  
 Kotilainen, J.K. & Falomo, R. 2004, *A&A*, 424, 107  
 Krist, J., Hook, R. 2004, <http://www.stsci.edu/software/tinytim>  
 Kukula, M.J., Dunlop, J.S., McLure, R.J., et al. 2001, *MNRAS*, 326, 1533  
 Lawrence, A. 1987, *PASP*, 99, 309  
 Lehnert, M.D., Miley, G.K., Sparks, W.B., et al. 1999, *ApJS*, 123, 351  
 Lister, M.L., Gower, A.C. & Hutchings, J.B. 1994, *AJ*, 108, 821  
 Lister, M.L. & Smith, P.S. 2000, *AJ*, 541, 66  
 McCarthy, P.J., van Breugel, W.J.M., Spinrad, H. & Djorgovski, S. 1987, *ApJ*, 321, L29  
 McCarthy, P.J., Miley, G.K., de Koff, S., et al. 1997, *ApJS*, 112, 415  
 McLeod, K.K. & McLeod, B.A., 2001, *ApJ*, 546, 794  
 McLure, R.J., Willott, C.J., Jarvis, M.J., et al. 2004, *MNRAS*, 351, 347  
 McLure, R.J., Kukula, M.J., Dunlop, J.S., et al. 1999, *MNRAS*, 308, 377  
 McLure, R.J., Dunlop, J.S. & Kukula, M.J. 2000, *MNRAS*, 318, 693  
 Magain, P., Courbin, F. & Sohy, S. 1998, *ApJ*, 449, 472  
 Marble, A.R., Hines, D.C., Schmidt, G.D., et al. 2003, *ApJ*, 590, 707  
 Martel, A.R., Baum, S.A., Sparks, W.B., et al. 1999, *ApJS*, 121, 81  
 Owen, F.N. & Puschell, J.J., 1984, *AJ*, 89, 932  
 Pavlovsky, C. et al. 2005, *ACS Data Handbook*, version 4.0 (Baltimore : STScI)  
 Peng, C., Ho, L.C., Impey, C.D. & Rix, H.-W. 2002, *AJ*, 124, 266  
 Percival, W.J., Miller, L., McLure, R.J. & Dunlop, J.S. 2001, *MNRAS*, 322, 843  
 Philipps, S., Boyce, P.J. 1992, *MNRAS*, 256, 673  
 Pian, E., Falomo, R., Hartman, R.C., et al. 2002, *A&A*, 392, 407  
 Price, R., Gower, A.C., Hutchings, J.B., et al. 1993, *ApJS*, 86, 365  
 Readhead, A.C.S., Pearson, T.J., Cohen, M.H., Ewing, M.S. & Moffet, A.T. 1979, *ApJ*, 231, 299  
 Reid, A., Shone, D.L., Akujor, C.E., et al. 1995, *A&A*, 110, 213  
 Rigler, M.A., Lilly, S.J. Stockton, A., Hammer, F. & Le Fèvre, O. 1992, *ApJ*, 385, 61  
 Rudy, R.J., Schmidt, G.D., Stockman, H.S. & Moore, R.L. 1983, *AJ*, 271, 59  
 Rusk, R. & Seaquist, E.R., 1985, *AJ*, 90, 30  
 Sanchez, S.F., Janhke, K., McIntosh, D.H., et al. 2004, *ApJ*, 614, 586  
 Schmidt, M. & Green, R.F. 1983, *ApJ*, 269, 352  
 Schmitt, H.R., Ulvestad, J.S., Kinney, A.L., et al. 2001, *ASPC*, 249, 230  
 Schultz, A. et al. 2005, *NICMOS Instrument Handbook*, version 8.0 (Baltimore : STScI)  
 Sérsic, J.L. 1968, *Atlas de Galaxias Australes*, Observatorio Astronomico, Córdoba  
 Siebenmorgen, R., Freudling, W., Krügel, E., Haas, M. 2004, *A&A*, 421, 129  
 Smith, J.E., Young, S., Robinson, A., et al. 2002, *MNRAS*, 335, 773  
 Smith, J.E., Robinson, A., Alexander, et al. 2004, *MNRAS*, 350, 140  
 Smith, J.E., Robinson, A., Young, S., Axon, D.J. & Corbett, E.A. 2005, *MNRAS*, 359, 846  
 Smith, P.S., Schmidt, G.D., Hines, D.C., Cutri, R.M. & Nelson, B.O. 2002, *ApJ*, 569, 23  
 Spencer, R.E., Schilizzi, R.T., Fanti, C., et al. 1991, *MNRAS*, 250, 225  
 Stockman, H.S., Angel, R.J.P. & Miley, G.K. 1979, *ApJ*, 227, L55  
 Tadhunter, C.N., Morganti, R., Robinson, A., et al. 1998, *MNRAS*, 298, 1035

- Tadhunter, C.N., Dickson, R., Morganti, R., et al. 2002, MNRAS, 330, 977  
Taylor, G.L., Dunlop, J.S., Hughes, D.H. & Robson, I.E. 1996, MNRAS, 283, 930  
Thompson, I.A. & Martin, P.G. 1988, ApJ, 330, 121  
Urry, M.C. & Padovani, P. 1995, PASP, 107, 803  
van Bemmell, I. M. & Bertoldi, F. 2001, A&A, 368, 414  
Veilleux, S., Kim, D.C., Peng, C.Y., et al. 2006, ApJ, 643, 707  
Véron-Cetty, M.P. & Véron, P. 2006, A&A, 455, 773  
Zakamska, N.L., Strauss, M.A., Krolik, J.H., et al. 2003, AJ, 126, 2125  
Zakamska, N.L., Schmidt, G.D., Smith, P.S., et al. 2005, AJ, 129, 1212  
Zakamska, N.L., Strauss, M.A., Krolik, J.H., et al. 2006, AJ, 132, 1496

**Table 2.** Results of our modelling of quasars host galaxy.

Name	$z$	QSO Type	Survey	Domain	Host Type	$b/a$	$PA_{host}$	Quality
2M 000810+1354	0.185	RQ	<i>Ma03</i>	Vis	S	0.62	137	1
PG 0026+129	0.142	RQ	<i>MI01</i>	NIR	E	0.86	113	1
PG 0043+039	0.385	RQ	<i>Bo98</i>	Vis	U	1.00	45	2
2M 005055+2933	0.136	RQ	<i>Ma03</i>	Vis	S	0.34	56	1
PG 0052+251	0.154	RQ	<i>Ba97</i>	Vis	S	0.70	171	1
PHL 909	0.171	RQ	<i>Ba97</i>	Vis	E	0.51	129	1
2M 010607+2603	0.411	RQ	<i>Ma03</i>	Vis	S?	0.31	115	1
SDSS J0123+0044	0.399	RQ	<i>Za06</i>	Vis	E	0.59	70	1
UM 357	0.335	RQ	<i>MI01</i>	NIR	E	0.75	62	1
2M 015721+1712	0.213	RQ	<i>Ma03</i>	Vis	U	1.00	65	2
PKS 0202-76	0.389	RL	<i>Bo98</i>	Vis	...	...	...	3
NAB 0205+02	0.155	RQ	<i>Ba97</i>	Vis	S	0.67	140	1
2M 022150+1327	0.140	RQ	<i>Ma03</i>	Vis	S?	0.62	142	1
2M 023430+2438	0.310	RQ	<i>Ma03</i>	Vis	...	...	...	3
0316-346	0.265	RQ	<i>Ba97</i>	Vis	...	1.00	90	2
2M 032458+1748	0.328	RQ	<i>Ma03</i>	Vis	...	...	...	3
2M 034857+1255	0.210	RQ	<i>Ma03</i>	Vis	U	1.00	104	2
PKS 0440-00	0.844	RL	<i>Ku01</i>	NIR	...	...	...	3
MS 07546+3928	0.096	RQ	<i>Bo98</i>	Vis	E	1.00	72	2
2M 092049+1903	0.156	RQ	<i>Ma03</i>	Vis	S	0.52	24	1
SDSS J0920+4531	0.402	RQ	<i>Za06</i>	Vis	E	0.55	160	1
PG 0947+396	0.206	RQ	<i>MI01</i>	NIR	S	0.71	22	1
HE 1029-140	0.086	RQ	<i>Ba97</i>	Vis	E	0.81	144	1
SDSS J1039+6430	0.402	RQ	<i>Za06</i>	Vis	E	0.88	20	1
PG 1048+342	0.167	RQ	<i>MI01</i>	NIR	S	0.65	94	1
SDSS J1106+0357	0.242	RQ	<i>Za06</i>	Vis	S	0.66	66	1
PG 1116+215	0.177	RQ	<i>Ba97</i>	Vis	E	0.81	65	1
PG 1121+422	0.234	RQ	<i>MI01</i>	NIR	...	...	...	3
PG 1151+117	0.176	RQ	<i>MI01</i>	NIR	E	0.87	149	1
PG 1202+281	0.165	RQ	<i>Ba97</i>	Vis	E	0.92	117	1
PG 1216+069	0.334	RQ	<i>Bo98</i>	Vis	...	...	...	3
3C 273	0.158	RL	<i>Ba97</i>	Vis	E	0.79	61	1
2M 125807+2329	0.259	RQ	<i>Ma03</i>	Vis	E	0.72	61	1
PG 1307+085	0.155	RQ	<i>Ba97</i>	Vis	U	1.00	105	2
2M 130700+2338	0.275	RQ	<i>Ma03</i>	Vis	E	0.82	178	1
PG 1309+355	0.184	RQ	<i>Ba97</i>	Vis	S	0.82	3	1
PG 1322+659	0.168	RQ	<i>MI01</i>	NIR	...	...	...	3
SDSS J1323-0159	0.350	RQ	<i>Za06</i>	Vis	E	0.71	26	1
PG 1352+183	0.158	RQ	<i>MI01</i>	NIR	E	1.00	139	2
PG 1354+213	0.300	RQ	<i>MI01</i>	NIR	E	0.78	166	1
PG 1358+043	0.427	RQ	<i>Bo98</i>	Vis	...	...	...	3
PG 1402+261	0.164	RQ	<i>Ba97</i>	Vis	S	0.61	170	1
SDSS J1413-0142	0.380	RQ	<i>Za06</i>	Vis	E	0.68	26	1
PG 1427+480	0.221	RQ	<i>MI01</i>	NIR	E	1.00	158	2
PG 1444+407	0.267	RQ	<i>Ba97</i>	Vis	S	0.82	48	1
2M 145331+1353	0.139	RQ	<i>Ma03</i>	Vis	S	0.57	179	1
2M 151621+2259	0.190	RQ	<i>Ma03</i>	Vis	S	0.51	47	1
2M 152151+2251	0.287	RQ	<i>Ma03</i>	Vis	U	1.00	2	2
2M 154307+1937	0.228	RQ	<i>Ma03</i>	Vis	U	0.82	30	1
3C 323.1	0.266	RL	<i>Ba97</i>	Vis	E	0.76	99	1
NAB 1612+26	0.395	RQ	<i>MI01</i>	NIR	E	0.55	99	1
Mrk 876	0.129	RQ	<i>MI01</i>	NIR	U	1.00	131	2
2M 163700+2221	0.211	RQ	<i>Ma03</i>	Vis	S	0.29	121	1
2M 163736+2543	0.277	RQ	<i>Ma03</i>	Vis	U	1.00	128	2
2M 165939+1834	0.170	RQ	<i>Ma03</i>	Vis	U	0.81	61	1
2M 170003+2118	0.596	RQ	<i>Ma03</i>	Vis	...	...	...	3
2M 171442+2602	0.163	RQ	<i>Ma03</i>	Vis	S	0.59	169	1
2M 171559+2807	0.524	RQ	<i>Ma03</i>	Vis	...	1.00	...	2
KUV 18217+6419	0.297	RQ	<i>MI01</i>	NIR	S?	1.00	65	2
3C 422	0.942	RL	<i>Ku01</i>	NIR	...	...	...	3

**Table 2.** continued.

Name	$z$	QSO Type	Survey	Domain	Host Type	$b/a$	$PA_{host}$	Quality
B2-2156+29	1.759	RL	<i>Ku01</i>	NIR	...	...	...	3
2M 222202+1959	0.211	RQ	<i>Ma03</i>	Vis	E?	1.00	46	2
2M 222554+1958	0.147	RQ	<i>Ma03</i>	Vis	S	0.49	141	1
PG 2233+134	0.325	RQ	<i>MI01</i>	NIR	E	1.00	135	2
2M 225902+1246	0.199	RQ	<i>Ma03</i>	Vis	E	0.68	69	1
2M 230304+1624	0.289	RQ	<i>Ma03</i>	Vis	U	1.00	50	2
2M 230442+2706	0.237	RQ	<i>Ma03</i>	Vis	E	0.77	60	1
2M 232745+1624	0.364	RQ	<i>Ma03</i>	Vis	S	0.62	76	1
2M 234449+1221	0.199	RQ	<i>Ma03</i>	Vis	...	...	...	3
SDSS J2358-0009	0.402	RQ	<i>Za06</i>	Vis	U	1.00	68	2

# Online Material



## Appendix A: Details on the observation campaigns used in this study

In this Appendix, we give some details about each of the observing campaigns used in this study and briefly described in Sect. 2.

### A.1. Sample of published and reliable data

#### A.1.1. The visible domain

**Ci93** (Cimatti et al. 1993) The sample defined in *Ci93* consists in a compilation of  $z \geq 0.1$  RGs studied in the literature who possess polarization measurements in the optical domain. Their total sample was made out of 42 RGs from which 8 NLRGs have  $z \in [0.5 - 1.2]$ . NLRGs possess an obvious host orientation in their rest-frame UV/blue (redshifted to optical) continuum images (*Ci93* and references therein). The  $\Delta\theta_O$  given in Tab. 1 of *Ci93* are the acute offset angle between the main orientation of their optical host image (our  $PA_{host}$ ) and the optical polarization angle  $\theta_{pola}$ .

**Di95** (Disney et al. 1995) The observations were made using the Planetary Camera (PC1) of the Wide Field & Planetary Camera2 (WFPC2, Bagget et al. 2002) on board of the HST. The PC1 is a 800 X 800 pixel camera and has a 0.046 arcsec per pixel resolution. Four quasars whose redshift  $z$  belongs to  $[0.25, 0.50]$  were imaged through the broadband F702W filter (which corresponds roughly to R band). The host galaxies parameters were derived using a two component cross-correlation technique which finds the best fit between the observed images and a series of galaxy templates (Phillipps & Boyce 1992).

**Dk96** (de Koff et al. 1996) The sample presented here is a part of a more extended sample, containing 267 3CR objects. In the sample of *Dk96*, 77 RGs at intermediate ( $0.1 < z < 0.5$ ) redshift were studied with the PC1 camera of the WFPC2 camera through the F702W filter. The host galaxy  $PA_{host}$  were determined by hand on the images by measuring the position angle of the largest extensions of the emission regions at a given surface brightness. The uncertainty in the derived position angles may thus be as large as  $15^\circ$  depending on the complexity of the objects.

**Le99** (Lehnert et al. 1999) 43 RLQs selected from the 3CR radio catalog and spanning a redshift range of  $z \in [0.3, 2.0]$  were imaged using the PC1 camera of the WFPC2 instrument on board of the HST. The observations were carried out in the F702W filter. The  $PA_{host}$  were estimated by fitting a series of ellipses on the residuals after the subtraction of a scaled Point Spread Function (PSF) playing the role of the unresolved nucleus. As for some objects the ellipticity of the isophotes can vary with radial distance to the center of the quasar, they defined the  $PA_{host}$  as the position angle of the major axis at a surface brightness of  $21.5 m_{F702W} \text{ arcsec}^{-2}$ . They estimated the uncertainty on the derived  $PA_{host}$  of less than  $20^\circ$  and an uncertainty of less than 0.07 on the ellipticity). Note that they do not provide  $b/a$  values in their Table 3 preventing us of using the  $b/a$  criterion for these objects. However this is not a problem since no  $PA_{host}$  are provided for the litigious objects. Moreover, we apply a redshift cut ( $z < 1.20$ ) in order to avoid the presence of tiny hosts for which the  $PA_{host}$  determination remains uncertain.

**Ma99** (Martel et al. 1999) 46 3CR radio galaxies were imaged thanks to the PC1 and the Wide Field (WF, the resolution of the WFs captors is  $0''.0996 \text{ pixel}^{-1}$ ) chips of the WFPC2 camera of HST through the F702W filter. The target were selected so that their redshift belong the range  $[0, 0.1]$ . They used the Vista command *axes* to calculate the flux-weighted position angle of the major axis and the ellipticity of the host galaxy.

**Du03** (Dunlop et al. 2003) For convenience, this sample gathers under the same name the published data by Dunlop et al. 2003 and McLure et al. 1999 because they are both taken from the same HST survey. 33 objects (RQQs, RLQs and RGs) with  $z \in [0.1, 0.25]$  were observed with the WF2 camera of the WFPC2 instrument through the F675W filter (corresponding roughly to R band). The parameters of the host galaxies were determined by fitting an analytical model to the PSF-subtracted images (McLure et al. 2000).

It is wise to pay attention to the fact that the values given in Table 3 of *Du03* do not fit the  $PA_{host}$  definition adopted here, contrary to what is claimed in the caption, but are determined with respect to the  $y$ -axis of the images. We have thus corrected these values applying a correction (the "ORIENTAT" parameter contained in the header of the observation files) taking account of the orientation of the HST with respect to the plane of the sky.

**Fi04** (Floyd et al. 2004) 17 quasars with  $z \in [0.29, 0.34]$  (both Radio-Loud and Radio-Quiet) were observed through the WF camera of the WFPC2 instrument on board of the HST. The observations were carried in two photometric bands (the broad F814W and narrow F791W filters roughly corresponding to I band) in order to avoid the contamination by strong emission lines depending on the redshift of the object. The procedure used to derive the host galaxies parameters is the same as used in *Du03*.

It is clearly stated that the position angles of the studied hosts are given anticlockwise from the vertical in the images. We thus corrected these values by the same way as those of *Du03* and derived the corresponding  $PA_{host}$ .

**Mc04** (McLure et al. 2004) 41 radio galaxies were observed in the I-band (F785LP filter) using the WF3 chip of the WFPC2. The redshift of the sample is comprised between  $0.4 < z < 0.6$ . The technique used to derive the host galaxies parameters is the same two-dimensional modelling process as the one used by *Du03*.

#### A.1.2. The near-IR domain

**Ta96** (Taylor et al. 1996) 44 quasars were observed in the photometric K-band ( $\lambda_{cent} \sim 2.2 \mu\text{m}$ ) using the IRCAM camera of the 3.9 m United Kingdom Infrared Telescope (UKIRT). The sample consists of RLQs, RQQs and RGs having a redshift around 0.2. Let us notice that the majority of these objets have been imaged in visible wavelengths by *Du03*. The parameters of the host galaxies were obtained using a fully two dimensional modelling procedure.

**Pe01** (Percival et al. 2001) 13 objects spanning a redshift range of  $[0.26, 0.46]$  were observed in the K-band using the IRCAM3 camera of the UKIRT telescope. As the observations were carried out from the ground for relatively distant objects, the host

galaxies are completely hidden by the PSF wings of the nuclear component. Each image was then deconvolved to subtract a nuclear PSF and recover the weak glare of the underlying host galaxy. The PSF-subtracted images were then modelled by a two dimensional brightness analytical galaxy profile. The orientation of the host galaxy (called  $\alpha$  by *Pe01*) is given in their Table 4. It is expressed in radians and related to the  $PA_{host}$  definition adopted in our paper following  $PA_{host} = \alpha$  (in degrees)  $+90$  (or  $PA_{host} = \alpha -90$  if  $\alpha$  (in degrees) is smaller than  $90^\circ$ ).

*Gu06* (Guyon et al. 2006) 32 quasars at  $z < 0.3$  selected from the Palomar-Green Bright Quasar Survey were imaged in the near infrared domain (H-band) using adaptive optics (AO) imaging with the Gemini 8.2 m and Subaru 8.1 m telescopes on Mauna Kea. The images were PSF-subtracted and residuals were modelled using analytical galaxy models.

*Ve06* (Veilleux et al. 2006) 33 quasars were observed in the H-band using the Near Infrared Camera and Multi Object Spectrometer (NICMOS) instrument on board of the HST. The sample consists of  $z < 0.3$  luminous late-stage galactic mergers. The removal of the PSF and the structural parameters of the underlying hosts were determined using the GALFIT (Peng et al. 2002) algorithm.

## A.2. Sample of new $PA_{host}$ data

### A.2.1. The visible domain

*Ba97* (Bahcall et al. 1997) The sample observed by *Ba97* contains 20 quasars  $z < 0.3$  (both RQQs and RLQs) imaged with the WF3 camera of the WFPC2 instrument through the F606W filter (whose spectral characteristics are  $\lambda_{cent} \sim 5900 \text{ \AA}$  and  $\Delta\lambda \sim 1500 \text{ \AA}$ ). Due to the redshift of the targets, powerful emission lines such as  $[OIII]$  and  $H_\alpha$  are included in the image. The objects in the sample come from the 1991 Véron-Cetty & Véron catalog and were selected such as  $z \leq 0.2$ ,  $M_V < -22.9$  et  $|b| > 35^\circ$  (where  $b$  stands for the galactic latitude). Several objects present in the sample were also part of the sample of *Du03* and were useful to assess our  $PA_{host}$  determination method (cf. Sect. 3.3.2).

*Bo98* (Boyce et al. 1998) 7 quasars were imaged with the WFPC2 instrument on board of the HST. Six of them were observed through the PC1 camera and the last one (PG0043+039) was observed using the WF chip. All the observations were taken through the F702W filter. The objects span a redshift range of  $0.09 < z < 0.43$  and contain both RLQs and RQQs.

*Ma03* (Marble et al. 2003) 29 RQQs spanning  $0.136 < z < 0.596$  were observed with the PC1 camera of the WFPC2 instrument through the F814W. The targets were selected from the Two Micron All Sky Survey (2MASS) essentially according to color and galactic latitude criterion. Note that the 2MASS sample contains reddened Type 1 quasars which, in the quasar unification scheme, can be interpreted as normal quasars, but seen close to the plane of an obscuring torus. The 2MASS objects have been classified as QSOs based on the fact that they are as luminous at  $2.2\mu\text{m}$  as QSOs in other samples (e.g. PG objects of comparable  $z$ ).

*Za06* (Zakamska et al. 2006) 9 Type 2 Radio-Quiet quasars at  $z \in [0.2, 0.4]$  were imaged through the Wide Field Channel (WFC) of the ACS instrument (Pavlovsky et al. 2005) in three photometric band (*Yellow*, *Blue* and *UV* cf. *Za06*). The resolution of the WFC is similar to the resolution of the PC1 camera of the WFPC2 instrument. Their targets were selected from the sample of Type 2 active galactic nuclei candidates unveiled by Zakamska et al. (2003) and Hao et al. (2005).

### A.2.2. The near-IR domain

*MI01* (McLeod et al. 2001) 16 RLQs were imaged in the near-infrared domain (with the F160W filter corresponding approximately to H band), using the NIC2 camera ( $0.075'' \text{ pixel}^{-1}$  resolution) of NICMOS on board of the HST. The objects have  $z < 0.4$  and were imaged in the MULTIACCUM mode (Schultz et al. 2005) which records data in a series of increasingly long nondestructive readouts, providing high dynamic unsaturated images.

*Ku01* (Kukula et al. 2001) 20 high redshift ( $z \in [0.83, 2.01]$ ) quasars were imaged using the NICMOS NIC1 camera (resolution of  $\sim 0.043'' \text{ pixel}^{-1}$ ). Due to the large redshift range, two filters were used to image the quasars near the same rest-frame wavelength and to avoid the presence of strong emission lines such as  $[OIII]$  and  $H_\beta$ . Thus the F110M filter (roughly J-band) was used to image the quasars in the  $z \in [0.83, 1.00]$  range, and the F165M (roughly H-band) filter to image the quasars in the  $z \in [1.67, 2.01]$  range.

## Appendix B: Comparison with previous studies

In this Appendix we give some details on the comparison of the results obtained with the modelling procedure adopted in this paper and the results derived in published papers (listed in Sect. 2) as five objects of our *new  $PA_{host}$  data* were previously studied. Hereafter, for each object of our sample being also part of another study where host parameters were determined, we give a brief description of the object and compare the derived  $b/a$  and  $PA_{host}$  obtained. In general we note a good agreement between both sets of parameters.

**PG 0052+251** The galaxy of this RQQ from the sample of *Ba97* consists in a spiral host with two prominent arms presenting several knots identified as *HII* regions. This object was already studied in two papers : Bahcall et al. 1996 (*Ba96*) and *Du03* (who noted that the galaxy profile was best modelled by a spheroidal component rather than a disk-like one). The results of these studies ( $PA = 173^\circ$  et  $b/a = 0.66$  for *Ba96* and  $PA = 175^\circ$  et  $b/a = 0.61$  for *Du03*) are very close to the one we obtain ( $PA = 171^\circ$  and  $b/a = 0.70$ ).

**PHL 909** This RQQ host observed by *Ba97* was characterized in two previous studies : *Ba96* and McLure et al. 1999 (referred as *Du03* in our study). The host parameters of the elliptical galaxy we obtained with our method ( $b/a = 0.51$  and  $PA = 129^\circ$ ) are similar to those found by both studies (*Ba96* found  $b/a = 0.5$  and  $PA = 138^\circ$  and *Du03*  $b/a = 0.61$  and  $PA = 131^\circ$ ).

**UM 357** This RQQ from the sample of NIR studied QSOs *MI01* has been previously studied from the ground in a similar waveband by *Pe01*. The derived parameters using our technique ( $PA = 62^\circ$  et  $b/a = 0.75$ ) are close to those obtained by *Pe01* ( $PA = 56^\circ$  and  $b/a = 0.66$ ).

**PG 1354+213** This RQQ was studied by *Pe01* in the K-band. In our sample, the observations of this object comes from the *MI01* H-band survey. As the two images were taken in Near-IR, we can generally expect a good match between the K-band and H-band galaxy parameters. This is effectively the case for this object for which *Pe01* gives  $PA = 169^\circ$  and  $b/a = 0.89$  while we obtain  $PA = 166^\circ$  and  $b/a = 0.78$ .

**PG 2233+134** The host galaxy parameters were formerly derived by *Pe01* in the near-IR. They obtained  $PA = 178^\circ$  and  $b/a = 0.8$ . These parameters are quite different from the one we obtained ( $PA = 135^\circ$  and  $b/a = 0.89$ ) using the *MI01* images. However, as mentioned in the Table 2 our results do not satisfy the quality criterion defined in the Sect. 3.3.2.